NTNU
Norwegian University of
Science and Technology

The propagation and energy losses of ultra high energy cosmic rays

Ingvild Olsen Lundanes

Physics
Submission date: May 2011
Supervisor: Michael Kachelriess, IFY

Norwegian University of Science and Technology
Department of Physics

The propagation and energy losses of ultra-high energy cosmic ray particles

Ingvild Olsen Lundanes

May 15, 2011

Department of Physics,
Norges teknisk-naturvitenskapelige universitet

***

Front cover illustration courtesy of the Pierre Auger Observatory, `auger.org`

PROBLEM DESCRIPTION

One of the most intriguing puzzles in contemporary astroparticle physics is the observation of air showers initiated by particles with energies beyond the cutoff predicted by Greisen, Zatsepin and Kuzmin. Compared to lower energies, the energy losses of protons increase sharply at $\approx 5 \cdot 10^{19}\,\mathrm{eV}$ since pion-production on cosmic microwave photons reduces their mean free path by more than two orders of magnitude.

Nuclei exhibit an even more pronounced cutoff at a somewhat higher energy, while photons are absorbed on a few Mpc due to pair-production on the radio background. Thus, the cosmic ray energy spectrum should steepen dramatically at $\approx 5 \cdot 10^{19}\,\mathrm{eV}$ and the sources of cosmic rays at higher energies should be within $\sim 100\,\mathrm{Mpc}$.

Only recently have observatories with detectors capable of registering a significant number of these rare particles been built. The aim of this project is to simulate the propagation of these ultra-high energy cosmic rays through space, in order to learn which starting conditions at the source give results most consistent with the data observed on Earth by the Pierre Auger Observatory.

This knowledge can hopefully be used to further the understanding of what the sources of ultra-high energy cosmic rays are.

ABSTRACT

This project investigates the propagation of ultra-high energy cosmic ray nuclei and protons. A simulation of the propagation subjecting the particles to energy losses due to cosmological redshift as well as interactions with the extra-galactic background radiation seeks to find the initial conditions at the source which give the best results on Earth compared to the observations of the Pierre Auger Observatory (PAO).

The results agree with previous works of the same kind that a chemical composition of medium-weight fits the observed air shower data best. The starting conditions which gave the best results for the air shower characteristics $\langle X_{\max} \rangle$ and RMS($X_{\max}$) were $\frac{dN}{dE} \propto E^{-\alpha}$ with $\alpha = 1.6$ for an initial chemical composition of 25% nitrogen and 75% silicon. Other combinations of the medium-weight nuclei also yielded similar results.

No starting conditions could accommodate both the observed $\frac{dN}{dE}$ and the air shower data simultaneously. Other works indicate that this might be improved by the implementation of extra-galactic magnetic fields, but it could also indicate that the error margins in the observed data are underestimated.

CONTENTS

1. INTRODUCTION TO COSMIC RAYS

1.1 A short overview of the history of cosmic ray research

The presence of a mysterious background of ionizing radiation has been known for a century, but its nature and origin is even today only partially understood. After his balloon flight in 1912 which revealed that this radiation *increased* with altitude, Austrian physicist V. F. Hess proposed that this radiation came, not from the crust of the Earth, but from outside the atmosphere. In 1926 Milikan was the first to call the radiation cosmic rays, as he believed it to be gamma rays because of the radiation's ability to penetrate the atmosphere [22].

Various experiments in the 1930s showed that the radiation was not photons, but charged particles. From the way them were affected by the Earth's magnetic field, they must be *positively* charged particles.

For example, more particles arrive from the west than east. This is because a particle travelling from the west towards the east parallel to the equator will be deflected down towards the Earth if its charge is positive, and upwards if negative. A positively charged particle arriving from the east however, will be deflected upwards. Thus the east-west effect can be explained if the cosmic ray particles are positively charged [23].

Before particle accelerators, cosmic rays were the only means particle physicists had of studying particles of extremely high energy, and so the early research on cosmic rays was mainly concerned with particle physics. After particle accelerators took over the experimental work of particle physics in the 1950s, cosmic ray research turned towards the astrophysics of cosmic rays [22]. The chemical composition, acceleration and propagation through the galaxy were studied, and today we have much more knowledge of these subjects than fifty years ago—at least for cosmic rays of more moderate energies.

The energy spectrum observed on Earth from cosmic rays follows a power law, though with some variations in the slope. This makes the highest energy cosmic rays difficult to study simply because there are so very few of them, and we have little data to work with. Only recently have observatories with detectors capable of registering a significant number of these rare particles been built.

The energy spectrum of cosmic rays follows a power law, with two changes

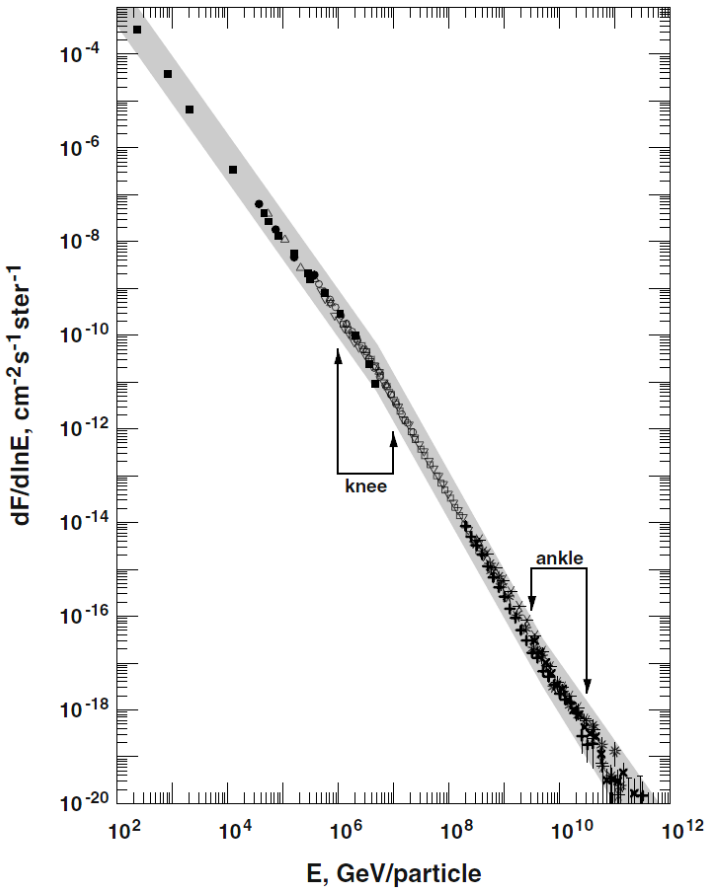

Fig. 1.1: The energy spectrum of cosmic rays, from Ref. [23].

in slope, often called the 'knee' and the 'ankle' of the spectrum because of its appearance when plotted. The knee is a steepening of the slope around 10^{15} eV and the ankle a flattening around $5 \cdot 10^{18}$ eV. Among the most widely accepted explanations for the knee, is that processes capable of accelerating particles up to the knee energy are more common than those who can accelerate particles to even higher energies, or that the knee is the energy at which a significant number of particles can escape the galaxy and thus never reach the Earth [13].

Less is known about the ankle than the knee, because of the aforementioned lack of data at these high energies. One possibility is that it marks the point where extragalactic cosmic rays start to dominate the spectrum, and that these follow a different spectrum than galactic ones [2]. The Greisen-Zatsepin-Kuzmin (GZK) limit (see Section 2.4.2) predicted in 1966 occurs shortly after the ankle, at $10^{19.5}$ eV. The prediction was that there would be a sharp drop in the number of particles above this energy, because at this energy protons become energetic enough to begin producing pions when interacting with the cosmic microwave background radiation (CMB).

For more detailed information on the history of cosmic ray research, see for example Elliot & Sekido's book [22]. More general information on cosmic rays can be found in Refs. [23] & [21].

1.2 The aim of the project

The subject of this project is the cosmic ray particles of the very highest energy, the ultra-high energy cosmic rays (UHECRs). The energy region we are studying is that from 10^{18} eV and up, which includes the ankle and the GZK limit. Particularly interesting is the region $10^{18.4} - 10^{20}$ eV, where we can compare with data from the Pierre Auger Observatory (PAO).

The propagation of UHECRs through the Universe is simulated by a Monte Carlo simulation. The particles will lose energy through cosmological redshift and interaction with the background radiation which is present everywhere, also in extragalactic space (the well-known cosmic microwave background is part of this background radiation). The energy losses can alter the energy spectrum of the particles, leading to a different spectrum here on Earth than the one with which they were injected at the source. Nuclei heavier than protons can also disintegrate into lighter particles when interacting with the background radiation, so the chemical composition will also change.

Knowledge about which starting parameters (energy spectrum and chemical composition) of the simulation that yields results closest to what is observed on Earth can aid in the quest for the sources of UHECRs. For example, if the best initial chemical composition is one consisting only of

protons, the sources are likely to be closer to us. This is because protons lose energy rapidly at high energies, due to pion production. In order to reach the Earth with an energy $E \sim 10^{19.5}$ for example, a proton cannot have propagated across more than $\sim 100\,\mathrm{Mpc}$.

On the other hand, particles with a small charge, like protons, will require longer distances in order to be isotropised by magnetic fields, while iron with 56 times the charge, will be isotropised quite quickly. Knowledge about the chemical composition of the UHECRs together with knowledge of the isotropy or anisotropy of their arrival directions can give information about the distance to the sources.

2. THEORY

2.1 Distance measurements

UHECR particles travel over cosmological distances, which complicates distance measurements and even the definition of the term "distance", as the expansion of the Universe becomes significant. When a particle propagates towards the Earth, the universe expands as it travels, increasing the distance the particle has to travel before it reaches the Earth. In this project the metric used is that of a flat Friedmann-Robertson-Walker metric.

$$ds^2 = -dt^2 + a^2(t)\left[d\chi^2 + \chi^2(d\theta^2 + \sin^2\theta\, d\phi^2)\right] \tag{2.1}$$

χ, θ and ϕ are the comoving coordinates, so named because they "move along" with the expansion of the universe, so that the comoving coordinates of a given point will remain unchanged as the universe expands. $a(t)$ is the scale factor, which denotes the scale of the universe at different times, with a_0, the value at the present, being normalised to unity.

The scale factor's time derivative divided by the scale factor itself is the Hubble parameter, which measures the speed of expansion at a given redshift (see below for a description of redshift). It has the unit of inverse time, but is often given as km/s per parsec.

$$\frac{\dot{a}}{a} = H(z) = H_0\sqrt{\Omega_{\mathrm{M}}(1+z)^3 + \Omega_{\Lambda}} \tag{2.2}$$

Ω_{M} and Ω_{λ} are the density parameters denoting the contributions to the Universe's total energy density from matter and vacuum energy. $\Omega_{\mathrm{M}}+\Omega_{\lambda} = 1$. In this project a cosmology with $H_0 = 75$ km/s/pc, $\Omega_{\mathrm{M}} = 0.3$ and $\Omega_{\lambda} = 0.7$ has been used. Detailed descriptions of FRW cosmological models can be found in works on general relativity, for example Ref. [10].

2.1.1 Redshift

The expansion of the universe means that every point in the universe can be said to be moving away from every other point. For photons or other particles this leads to a *redshift*, a decrease in a particle's momentum, similar

to the Doppler effect which occurs when waves are emitted from moving sources. Since sources further away from us move away with a higher velocity, redshift increases with distance and can be used as an observable distance measurement. The relationship between redshift of a photon emitted at time t and the expansion of the universe can be expressed by the scale factor $a(t)$.

$$1 + z(t) = \frac{a_0}{a(t)} \tag{2.3}$$

2.1.2 Comoving distance

The comoving distance between two points is defined as the integral over the comoving coordinates in the metric (Eq. (2.1)) in the path of a photon. Photons travel along $ds^2 = 0$, and for the radial distance $d\theta = 0$ and $d\phi = 0$. The comoving distance D_{C} as a function of the time t, the time at which a photon which reaches us now (at t_0), was emitted from the source at distance $D_{\mathrm{C}}(t)$, is then given by [5]

$$D_{\mathrm{C}}(t) = c \int_t^{t_0} \frac{dt'}{a(t')} \tag{2.4}$$

From Eq. (2.3) we find that

$$\frac{dt}{a(t)} = -\frac{a(t)dz}{\dot{a}a_0} = -\frac{dz}{a_0 H(z)} \tag{2.5}$$

Substitution then gives

$$D_{\mathrm{C}}(z) = c \int_0^z \frac{dz'}{H(z')} \tag{2.6}$$

2.1.3 Lookback distance

The lookback time t_{L} is the time light uses to travel from a source to an observer, while the universe expands. The lookback distance D_{L} is then the lookback time multiplied by c. Using Eq. (2.3) again, we have

$$\frac{dz}{dt} = -\frac{H(z)}{a(t)} = -(1+z)H(z) \tag{2.7}$$

which gives a lookback time [11]

$$t_{\mathrm{L}}(z) = \int_0^z \frac{dz'}{(1+z')H(z')} \tag{2.8}$$

2.2 Sources of ultra-high energy cosmic rays

Little is known about the sources of ultra-high energy cosmic rays, and the goal of this project is to learn more about which source conditions yield the best results for the UHECR spectrum observed on Earth. The main variables are the energy spectrum and chemical composition of the particles injected at the source. The sources have been assumed to be uniformly distributed in comoving distance from the Earth. This assumes that there is a constant density of sources throughout space. The flux from each source decreases as $\frac{1}{r^2}$, while the number of sources at a given distance increases like r^2, giving a uniform distribution in comoving distance.

Since the energy spectrum of cosmic rays observed on Earth closely follows a power law spectrum, with a few changes in slope, the sources are assumed to accelerate particles to an energy spectrum

$$\frac{dN}{dE} \sim E^{-\alpha}, \quad E_{\min} < E < E_{\max} \tag{2.9}$$

with $E_{\min} = 10^{18}\,\text{eV}$ and $E_{\max} = 10^{20.5} - 10^{22}\,\text{eV}$. $E_{\min}$ is chosen because energies below $10^{18}\,\text{eV}$ aren't relevant in this project, which seeks to study the energy spectrum after the ankle, while $E_{\max}$ should represent a possible maximum energy, above which the source cannot accelerate particles.

Possible sources of UHECRs up to energies slightly above $10^{20}\,\text{eV}$ include active galactic nuclei, large-scale shocks, gamma ray bursts and pulsars among others [23], and $10^{20.5}\,\text{eV}$ is the more realistic maximum energy. $10^{22}\,\text{eV}$ is tested in case there are more powerful acceleration processes.

A range of different initial chemical compositions are also investigated, with varying amounts of protons, medium-light, medium-heavy and heavy nuclei. The highest energy cosmic rays are not necessarily only protons, as nuclei are easily accelerated in electromagnetic fields, but also lose energy rapidly during propagation (see Fig. 2.1). Therefore both protons and nuclei are considered.

2.3 Electromagnetic fields

Since cosmic rays are charged particles, they are affected by electromagnetic fields. The effects of electromagnetic fields on propagation were not implemented in this simulation, but a discussion of them is still relevant. Since the Lorentz force

$$\vec{F} = q(\vec{E} + \vec{v} \times \vec{B}) \tag{2.10}$$

is proportional to the particle's charge q ($\vec{E}$ and $\vec{B}$ are the electric and magnetic fields, respectively, and $\vec{v}$ the particle's speed), nuclei of high charge

are affected more strongly by electromagnetic fields. A source with an electromagnetic field of a given strength can accelerate iron nuclei to higher momenta than protons for instance.

The radius of the circular path of a charged particle in a magnetic field, the Larmor radius, is inversely proportional to charge.

$$r = \frac{p}{qB} \tag{2.11}$$

p is the particle's momentum and B is the size of the transverse component of the magnetic field. A shorter Larmor radius means a stronger deflection in magnetic fields.

For propagation, this means that the particles of higher charge will travel a longer distance before they reach their destination, as their path differs more from a straight line. A larger deflection also means that the particles' arrival directions will be isotropised more quickly. If the arrival directions of particles with a certain energy are isotropic, the particles must have travelled far enough for deflection in magnetic fields to distribute the arrival directions randomly, which can indicate how far away the sources are.

2.4 Energy loss processes

There are three main processes through which cosmic rays lose energy as they propagate through intergalactic space. Firstly, all particles will lose energy as they are redshifted because of the expansion of the universe. At a given redshift z this loss is a constant (ie. not energy-dependent) fraction of the particle's energy per time.

This can easily be found using the fact that a particle of energy E will lose energy when it is redshifted as

$$E(z) = \frac{E}{1+z} \tag{2.12}$$

Differentiating Eq. (2.12) with respect to time, using Eq. (2.3) for the time-dependence of z, we get

$$\beta_{\mathrm{rsh}}(z) = \frac{1}{E(z)}\frac{dE(z)}{dt} = H(z) = H_0\sqrt{\Omega_{\mathrm{M}}(1+z)^3 + \Omega_{\lambda}} \tag{2.13}$$

2.4.1 Pair production

Particles of high energy, like the ones we are concerned with here, will also lose energy through pair production.

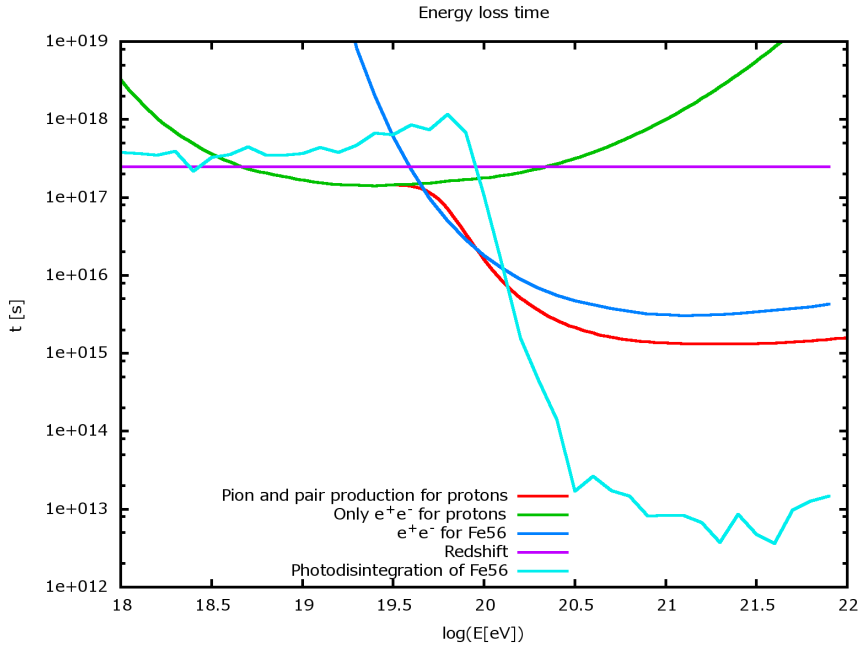

Fig. 2.1: Energy loss time for ^{56}Fe due to different processes

Production of e^+e^- pairs is a significant cause of energy loss throughout the energy range of UHECRs, peaking around $10^{19.4}$ for protons. It occurs when a free proton, or a nucleon in a nucleus, interacts with the cosmic background radiation (see Section 2.4.4), creating an electron-positron pair. The threshold for the reaction $A + \gamma \to A + e^+ + e^-$ is that $E'_\gamma > 2m_e c^2 = 1.022\,\mathrm{MeV}$, in the rest frame of the particle A[1]. If a photon has energy E_γ in the lab frame, its energy in the rest frame of A is

$$E'_\gamma = \gamma E_\gamma (1 + \beta \cos\theta) \tag{2.14}$$

where γ is the Lorentz factor of particle A, $\beta = \frac{v}{c}$ and θ is the angle of the photon's direction, so that $\theta = 0$ for a heads-on collision. Since $\gamma \sim 10^9$ for a proton of energy $10^{18}\,\mathrm{eV}$, a typical CMB photon of $E_\gamma \sim 10^{-3}\,\mathrm{eV}$ will have $E'_\gamma \sim 2\,\mathrm{MeV}$ even for the lowest particle energy in this project.

A detailed calculation of the energy loss due to e^+e^- production can be found in Blumenthal's 1970 paper [4]. The result is:

$$-\frac{dE}{dt} = \alpha r_0^2 Z^2 (m_e c^2)^2 \int_2^\infty d\xi n \left(\frac{\xi m_e c^2}{2\gamma}\right) \frac{\phi(\xi)}{\xi^2} \tag{2.15}$$

[1] This is intuitive, but can be proven for example through the conservation of the invariant four-momentum squared, $p_\mu p^\mu$.

ϕ is a function of the process' cross section, and n is the number density of photons as a function of photon energy. The integration variable ξ is integrated from 2 to ∞, ensuring integration from the threshold $2m_{\mathrm{e}}c^2$ in photon energy. r_0 is the classical electron radius, and Z the charge of A. This function can only be evaluated numerically, and depends on the energy of the particles, as this affects the cross section, and the distribution of background photons.

2.4.2 Pion production

At sufficiently high energies, cosmic rays can also lose energy through photo-pion production. This happens when a UHECR proton collides with background photons, $p + \gamma \rightarrow \pi^+ + n$ and $p + \gamma \rightarrow \pi^0 + p$. A detailed description of pion production can be found in Ref. [24], which finds that the energy loss of a CR proton for pion production is

$$\beta_\pi = \frac{1}{E}\frac{dE}{dt} = \frac{c}{2\gamma^2}\int_{\epsilon_{\mathrm{th}}/2\gamma}^{\infty} d\epsilon \epsilon^{-2} n(\epsilon) \int_{\epsilon'_{\mathrm{th}}}^{2\gamma\epsilon} d\epsilon' \epsilon' \sigma(\epsilon') K(\epsilon') \tag{2.16}$$

where K is the inelasticity of the interaction and ϵ_{th} is the threshold energy.

The threshold for this process can be found in the same way as for pair production, by using the fact that $p_\mu p^\mu$ is conserved in the process, and Lorentz invariant.

In the following calculation, primed quantities are before the collision, in the rest frame of the initial proton, while unprimed quantities are after the collision, in the centre of mass frame where $\vec{p}_{tot} = 0$. We calculate the threshold for $p + \gamma \rightarrow \pi^0 + p$, as π^0 is the lighter of the pions. At the threshold all particles are at rest after the collision, and $E = \gamma mc^2 \rightarrow E = mc^2$. For simplicity we use natural units in the calculation, $c = 1$.

$$\begin{aligned} p'_\mu p'^\mu &= p_\mu p^\mu \\ (E'_\gamma + m_{\mathrm{p}})^2 - \vec{p'}_\gamma^{\,2} &= (m_{\mathrm{p}} + m_\pi)^2 \\ E'_\gamma &= m_\pi(1 + \frac{m_\pi}{m_{\mathrm{p}}}) \approx 155\,\mathrm{MeV} \end{aligned} \tag{2.17}$$

Assuming a heads-on collision between a photon and a proton with $\beta \approx 1$, we get from Eq. (2.14) and (2.17) that the required Lorentz factor of the proton is $\gamma = \frac{E'_\gamma}{2E_\gamma} = 7.75 \cdot 10^{11}$ for a CMB photon of energy $E_\gamma \sim 10^{-3}\,\mathrm{eV}$. This corresponds to $E_{\mathrm{p}} \sim 7 \cdot 10^{19}\,\mathrm{eV}$. As there are background photons of higher energies as well, pion production begins around $E_{\mathrm{p}} \sim 10^{19.5}\,\mathrm{eV}$.

For a nucleus with mass number A, the energy of the individual nucleons is $E_N = E_A/A$. This means that in the energy range of UHECRs,

$10^{18} < E < 10^{21}$, this energy will be below the pion production threshold for most heavy nuclei.

Above the threshold, the cross section for photo-pion production rises rapidly with E'_γ into a sharp peak around the region of the 1232 MeV Δ-baryon, an unstable pion-nucleon resonance state, before falling off again.

The energy loss due to pion production therefore peaks quite soon after its threshold, and as can be seen from Fig. 2.1, pion production leads to large energy losses. It was this which lead Greisen, Zatsepin and Kuzmin to predict a cutoff in the energy spectrum of UHECRs, today known as the GZK limit. Any particle with energy $E \gtrsim 10^{19.5}\,\text{eV}$ should lose its energy so rapidly that it will not be able to travel long distances ($\sim 100\,\text{Mpc}$) before it has lost a significant amount of energy. Thus, we should observe very few particles above this energy on Earth, giving a sharp steepening of the energy spectrum [9].

2.4.3 Photodisintegration

Nuclei which consist of more than one nucleon can also disintegrate into several particles, through interaction with the cosmic background radiation. This process is treated in some detail in Ref. [25] & [20], where it is shown that the rate of photodisintegration for a nucleus A, emitting i nucleons is

$$R_{A,i} = \frac{1}{2}\gamma_A^{-2} \int_0^\infty d\epsilon \epsilon^{-2} n(\epsilon) \int_0^{2\gamma_A \epsilon} d\epsilon' \epsilon' \sigma_{A,i}(\epsilon') \tag{2.18}$$

where ϵ' is the photon energy in the rest frame of the nucleus, σ is the process' cross section and $n(\epsilon)$ again is the photon number density.

This process is a significant source of energy loss in the energy range from the giant dipole resonance[2] to the threshold for pion production. In terms of the energy of the photon in the rest frame of the nucleus (see Eq. (2.14)), this energy range is $25\,\text{MeV} \lesssim E' \lesssim 155\,\text{MeV}$

2.4.4 The photon background

All the energy loss processes discussed here, with the exception of losses due to redshift, involve the cosmic ray particles interacting with the background radiation. The rate of energy loss for each process therefore depends on the number density of background photons of different energies. It is difficult to determine the extragalactic background, as foreground radiation from our galaxy makes it hard to separate out the background radiation. Several

[2] A resonance state where, as in the case of the Δ-baryon resonance, the cross section peaks sharply.

different models for this background radiation have been in use, and the energy losses of UHECRs then depend on which model is used.

In this project, the 2010 results of Kneiske *et.al.* [15] have been used. This model includes more of the background radiation than only the well-known CMB—primarily in the optical and infrared.

2.5 Cosmic rays in the Earth's atmosphere

With the extremely low flux of UHECRs reaching the Earth[3], it is not feasible to observe the particles directly. However, when the cosmic ray particles enter the atmosphere they initiate showers of particles created in electromagnetic and hadronic cascades, which in turn *can* be observed from the ground.

When cosmic rays enter the atmosphere they interact with atmospheric molecules to produce secondary particles, which primarily are pions [23]. As pions are unstable, with a mean lifetime of $\tau = 2.6 \cdot 10^{-8}\,\mathrm{s}$ for charged pions and $\tau = 8.4 \cdot 10^{-17}\,\mathrm{s}$ for neutral pions [8], the pions can either re-interact or decay into photons (π^0) or muons (π^+/π^-). A cascade initiated by a cosmic ray proton or nucleus will thus consist of both electromagnetic cascades and hadronic cascades. These large cascades, called extensive air showers (EAS), were discovered in the 1930s by Pierre Auger *et.al.* [3].

EAS are characterised by the number of particles in the shower at a certain depth in the atmosphere, $N(X)$, particularly by where this function reaches its maximum. Because of the many possible ways a shower can develop, EAS are characterised by the average depth of the maximum, $\langle X_{\max} \rangle$ and the variability in the position of the maximum, given as the root mean square deviation from this average $\mathrm{RMS}(X_{\max})$. The depth is measured in $\mathrm{g/cm^2}$, the integrated density of the atmosphere at the relevant depth. Since the atmosphere is denser closer to the ground, a higher value of X means shorter distance from the ground, that is, deeper into the atmosphere.

An approximate value of $X_{\max}$ can be calculated from

$$\langle X_{\max} \rangle = \alpha(\ln E - \langle \ln A \rangle) + \beta \tag{2.19}$$

where α and β are parameters which depend on the hadronic interaction model [16]. No simple approximation exists for $RMS(X_{\max})$, but it also decreases with increasing A, though not as quickly as $\frac{1}{\sqrt{A}}$ [27]. Both quantities increase with higher energy, and decrease with higher A.

Calculating $\langle X_{\max} \rangle$ and $\mathrm{RMS}(X_{\max})$ for a shower initiated by a given particle is a complex task for such large cascades as the EAS, and is usually

[3] The data from PAO in 2008 consisted of slightly less than 20 000 events after approximately 4 years of observation [26].

done by using different Monte Carlo simulations. A complete calculation would require enormous amounts of computing time, and the simulations therefore use different methods of simplifying the calculation, for example by combining Monte Carlo simulations with numerical solutions. The results depend both upon which simulation model is used, and also the physics content of the models, where the model describing hadronic interactions is the least certain [18]. In this project the simulations QGSJET [14], QGSJET-II [17] and SIBYLL [1] have been used to give a range of possible values for $\langle X_{\max} \rangle$ and RMS($X_{\max}$) for a given UHECR composition entering the Earth's atmosphere.

The observatories who measure the EAS data also use models to determine $\langle X_{\max} \rangle$ and RMS($X_{\max}$) from raw observational data. The EASs consist of a very large number of particles spread over a large area before they hit the ground, and only some of these are detected. From those, the characteristics of the shower are reconstructed [27].

2.6 Statistical test

When comparing the results of the simulation with the data set from the Pierre Auger Observatory (PAO), a goodness of fit test is used, which is based on the fact that the variable

$$\chi^2 = \sum_{i=1}^{k} \frac{(o_i - e_i)^2}{e_i} \tag{2.20}$$

behaves like a random variable from a chi-squared probability distribution with $k-1$ degrees of freedom. o_i is the observed value, from PAO, and e_i is the expected value if the hypothesis being tested is true, which is this case means the value from the Monte Carlo simulation. This is only valid if $e_i \gtrsim 5, \ \forall \ i$, which means that the energy bins above $\log(E) = 19.8$ have to be combined into one, to ensure that the criterion is met.

It is intuitive that a lower value of χ^2 is equivalent to a better fit, as this corresponds to a smaller difference between the expected and observed values. For a significance level α (the probability of rejecting a hypothesis which is true), the hypothesis is rejected if $\chi^2 > \chi^2_\alpha$.

This description of the goodness to fit test is based on its description in Ref. [28].

3. COMPUTER MODELLING OF COSMIC RAY PROPAGATION

The source code for this project is not printed due to its length, it is available from the author upon request.

3.1 Sources

The goal of this project has been to model the energy loss of UHECR particles as they propagate towards the Earth, in the hope that information about the energy spectrum and chemical composition of the injected particles that produce results most similar to those seen on Earth can lead to a better understanding of the sources of UHECRs.

In this simulation, sources of UHECRs are assumed to be distributed with a constant density in space. As the number of sources within a spherical shell centred on the Earth increases with the radius of this shell at the same rate as the flux from each source decreases, the sources can be considered to be uniformly distributed in comoving distance from the Earth. Direction is not considered here, only distance.

A source distance is selected randomly between redshift 0 and $z_{\max} = 1.0$. Then the energy of the injected particle is chosen from the energy spectrum $\frac{dN}{dE} \propto E^{-\alpha}$, between $E_{\min} = 10^{18}\,\text{eV}$ and $E_{\max} = 10^{20.5} - 10^{22}\,\text{eV}$. In previous works of this kind, α has ranged from 1.6 which gave the best results for medium heavy nuclei in Hooper and Taylor's paper from 2010 [12] to 2.6 which was the best fit for protons in DeMarco *et.al*'s work in 2003 [6]. The chemical composition of the injected particles and the value of α are the main parameters that are adjusted in the search for a good fit to the data observed on the Earth.

In this simulation, all particles are given energies from the same energy spectrum. This is a simplification because, as mentioned in Section 2.3, the electromagnetic force on a particle is proportional to its charge. It would be more realistic to give the particles energies from an energy spectrum where $E_{\max}$ is charge-dependent.

Since there are many different chemical compositions possible, four ele-

ments have been chosen to represent the different possibilities. Only elements which can be produced in stellar fusion are considered (ie. up to and including ^{56}Fe), as heavier elements are less abundant. Protons represent the lightest nuclei, ^{15}N and ^{28}Si the medium-weight nuclei and ^{56}Fe the heaviest. The compositions tested were 20-100% (in 20% increments) one of the three heavier nuclei, with the remainder being protons, as well as mixtures of three or all four types of nuclei and 50% of each of two elements.

3.2 Monte Carlo simulation of energy losses and disintegration

The particle is then propagated towards the Earth, losing energy due to the expansion of the universe, pair and pion production and photodisintegration (in the case of nuclei). Due to the very high energies of the particles involved, they are assumed to travel at the speed of light. Losses due to redshift, pair and pion production are treated as continuous in each step of the Monte Carlo simulation. In the case where a nuclei which can disintegrate is being propagated, the distance the nuclei must travel before losing 1% of its energy is calculated. Code provided by Askhat Gazizov calculates the average interaction length and branching ratios for a given nuclei of given energy and redshift. From the average interaction length a random interaction point is chosen from an exponential distribution $p_{\mathrm{int}}(x) \sim e^{-x/l_{\mathrm{int}}}$. If this point is before the nuclei has lost 1% of its energy, the nuclei disintegrates here choosing a random branch with the probabilities calculated along with l_{avg}. The interaction length is highly dependent on the particle's energy, especially at high energies (see Fig. 3.1), so if the particle does not interact before 1% energy loss, the interaction length is recalculated using the new, lower energy and the process repeated.

In this simulation a simple approximation of disintegration is used where the initial nucleus' energy is divided equally among its nucleons, so that if ^{56}Fe disintegrates into ^{55}Mn + p, $E_{\mathrm{Mn}} = \frac{55}{56}E_{\mathrm{Fe}}$ and $E_p = \frac{1}{56}E_{\mathrm{Fe}}$. Both particles are assumed to continue in the direction of the Earth. Neutrons are treated as protons in this simulation, and we do not consider electrons.

Photodisintegration creates a shower of multiple particles. All nuclei and protons/neutrons in this shower are considered, and propagated towards the Earth, as long as their energy remains in the energy range in which we are interested. Particles below $E = 10^{18}$ eV are discarded.

The energy losses which are, or are treated as, continuous are calculated from tabulated values of $\beta = \frac{1}{E}\frac{dE}{dt}$. The code which generates these tables have been supplied by Michael Kachelrieß. This fractional energy loss can be integrated over a redshift interval rather than a time interval through a

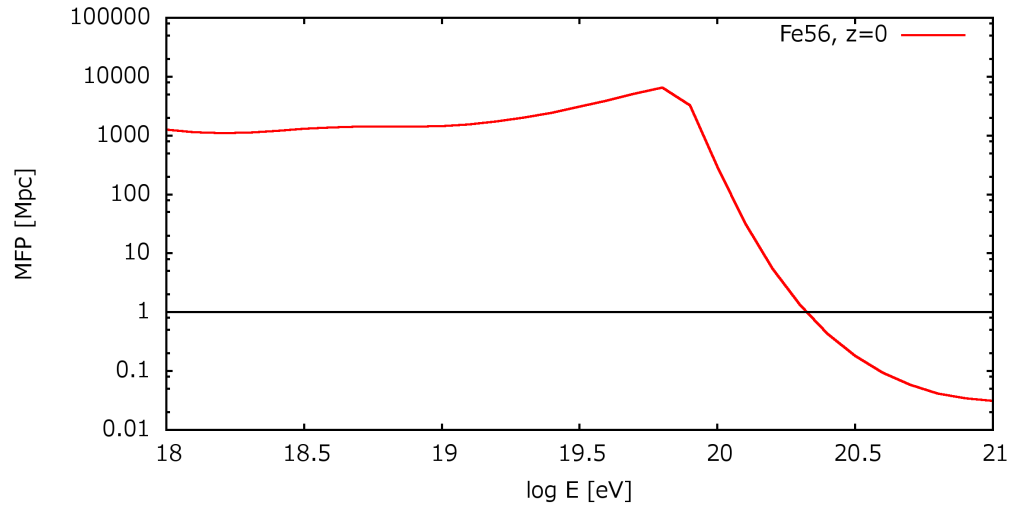

Fig. 3.1: The mean free path for photodisintegration of Fe56.

change of variables which makes use of the fact that for a particle travelling at the speed of light, $\frac{dt}{dz}$ is $\frac{dt_{\mathrm{L}}}{dz}$, the lookback time discussed in Section 2.1. The integration is then done with the routine *qsimp* from Numerical Recipes [19] which is based on Simpson's rule.

The tabulated values of β are for $z = 0$. A particle which arrives at Earth now, after having travelled from a source at a given z, left the source a significant amount of time ago. This means that when the particle was at redshift z, the density of the background photons and higher, as was the energy of each photon, since the Universe then had not yet expanded to its current size. This is accounted for by using

$$\beta(E, z) = (1 + z)^3 \beta((1 + z)E, 0) \tag{3.1}$$

the factor $(1 + z)^3$ accounts for the higher density, while the factor $(1 + z)$ accounts for the higher energy.

The tabulated values of β for pair production are calculated for protons. The value for a heavier nuclei is approximated as the value for a proton multiplied by the nucleus' charge Z^2 (see Eq. (2.15)). For a nucleus A, the energy of each individual nucleon is $E_N = E_A/A$, so that the relevant value for $\left(\frac{dE(E)}{dt}\right)_A \sim \left(\frac{dE(E/A)}{dt}\right)_{\mathrm{p}}$. Finally, we must consider that the tabulated values are $\frac{1}{E}\frac{dE}{dt}$, not $\frac{dE}{dt}$. In the factor $\frac{1}{E}$, the correct energy to use is the energy of the nucleus, not that of the individual nucleons. The end result is then

$$\beta(E, z, A) = \frac{Z^2}{A} \beta(E/A, z, 1) \tag{3.2}$$

3.3 The results observable on Earth

When all the particles in the shower has reached $z = 0$, the energy and atomic weight of each is stored. When 1 000 000 initial particles have been propagated to the Earth and the total number of events in the energy range of the PAO data ($10^{18.4} - 10^{20.5}$eV) is normalised to the same number as in PAO's data set (19582). The flux $\frac{dN}{dE}$, $\langle A \rangle$ and the chemical composition at different energies are printed to file, with logarithmic energy bins ($\log(E) = 18.4, 18.5, 18.6$ etc.).

The resulting EAS is also calculated, using code provided by Sergey Ostapchenko. For ease of calculation, all possible nuclei are divided into groups, represented by one type of nucleus. The same representative nuclei are used as for the injected particles. Particles of $A \leq 4$ are represented by protons, $9 \leq A \leq 19$ by ^{15}N, $20 \leq A \leq 39$ by ^{28}Si and $A \geq 40$ by ^{56}Fe. For each energy bin $\frac{N_i}{N}$ is calculated, where N is the total number of particles in the bin, and N_i is the number of particles represented by either of the four nuclei mentioned above. As the different EAS models give different results (see Section 2.5), a range of possible values of $\langle X_{\max} \rangle$ and RMS($X_{\max}$) are calculated for each energy bin.

The results obtained are then compared to the data from PAO. The energy spectrum is compared by doing a goodness of fit test on the number of events per energy bin with significance level 0.05, with the PAO data as the observed, and the simulated data as the expected values.

For the comparison of $\langle X_{\max} \rangle$ and RMS($X_{\max}$), the testing is complicated by the fact the the simulation yields a range of values, rather than one single value per bin. Here we have chosen to set the contribution to χ^2 to zero when the PAO value is within this range, and to set $o_i - e_i$ equal to the difference between the PAO value and the value in the simulated range which is closest to the PAO value, in the case where PAO's value is outside the range given by the simulation.

3.4 External code

This simulation has also made use of code not written by the author. For numerical calculations, routines from Numerical Recipes have been used. The source code for these routines is copyrighted. It can be found in Numerical Recipes third edition [19]. The routines used are:

- *qsimp* — numerical integration routine based on Simpson's rule
- *Linear_interp* — piecewise linear interpolation

- *Ran* — random number generator
- *Expondev* — random number generator, exponential deviates

Sergey Ostapchenko contributed the code used to calculate the $\langle X_{\max} \rangle$ and $RMS(X_{\max})$ of air showers initiated by a given particle. Askhat Gazizov provided the code used to simulate photodisintegration—calculation of the mean free path of a given particle and its branching ratios. Michael Kachelrieß provided the code used to generate the tabulated values of β for pair and pion production.

4. RESULTS

The simulation of UHECR propagation gives three types of results, the energy spectrum of particles arriving on Earth, $\frac{dN}{dE}$, and data about the EAS characteristics, $\langle X_{\max} \rangle$ and $RMS(X_{\max})$. These are compared to data from the Pierre Auger Observatory. But in order to check how realistic the results are, it is not sufficient to check the results against the observational data. Several checks can be done to see if the simulation behaves as expected.

Please note that "chemical composition" in this project can refer to either the initial chemical composition of the particles which leave the source, or the chemical composition observed on Earth, which will differ from the initial one because of photodisintegration. Hopefully the text makes it clear which is meant.

4.1 Tests

The simulation of energy loss is tested by injecting a particle with $E = 10^{18}$, $10^{18.1}$, $10^{18.2}$, ... ,10^{22} eV and propagating it over a short redshift interval, $\Delta z = 0.00001$[1], and calculating $\frac{\Delta E}{\Delta t}$, where ΔE is the difference between initial and final energy, and Δt is the time the particle uses to travel the distance at the speed of light. $\frac{\Delta E}{\Delta t}$ can then be compared to previously found values of $\frac{dE}{dt}$. In Fig. 4.1 the energy loss time ($\left[\frac{1}{E}\frac{dE}{dt}\right]^{-1}$) is plotted next to the results of Puget *et.al* [20]. It should be noted that the calculations in the 1976 paper were based on a different value of H_0 ($H_0^{-1} = 6.17 \cdot 10^{17}$ s, as noted on the plot) and a different model of the background radiation. However, the shape of the functions are in agreement.

For photodisintegration, $\frac{\Delta E}{\Delta t}$ is defined as the difference in energy between the initial particle and the final state particle of highest energy, divided by the time it takes before the particle interacts. Since there is an element of randomness in the photodisintegration process, which is not continuous, the average value of $\frac{\Delta E}{\Delta t}$ for 10 000 000 particles was used. The energy loss time for photodisintegration can be compared to the mean free path for the same

[1] For practical reasons, the calculation was done between $z = 0.9$ and $z = 0.89999$, rather than between $z = 0.00001$ and $z = 0$.

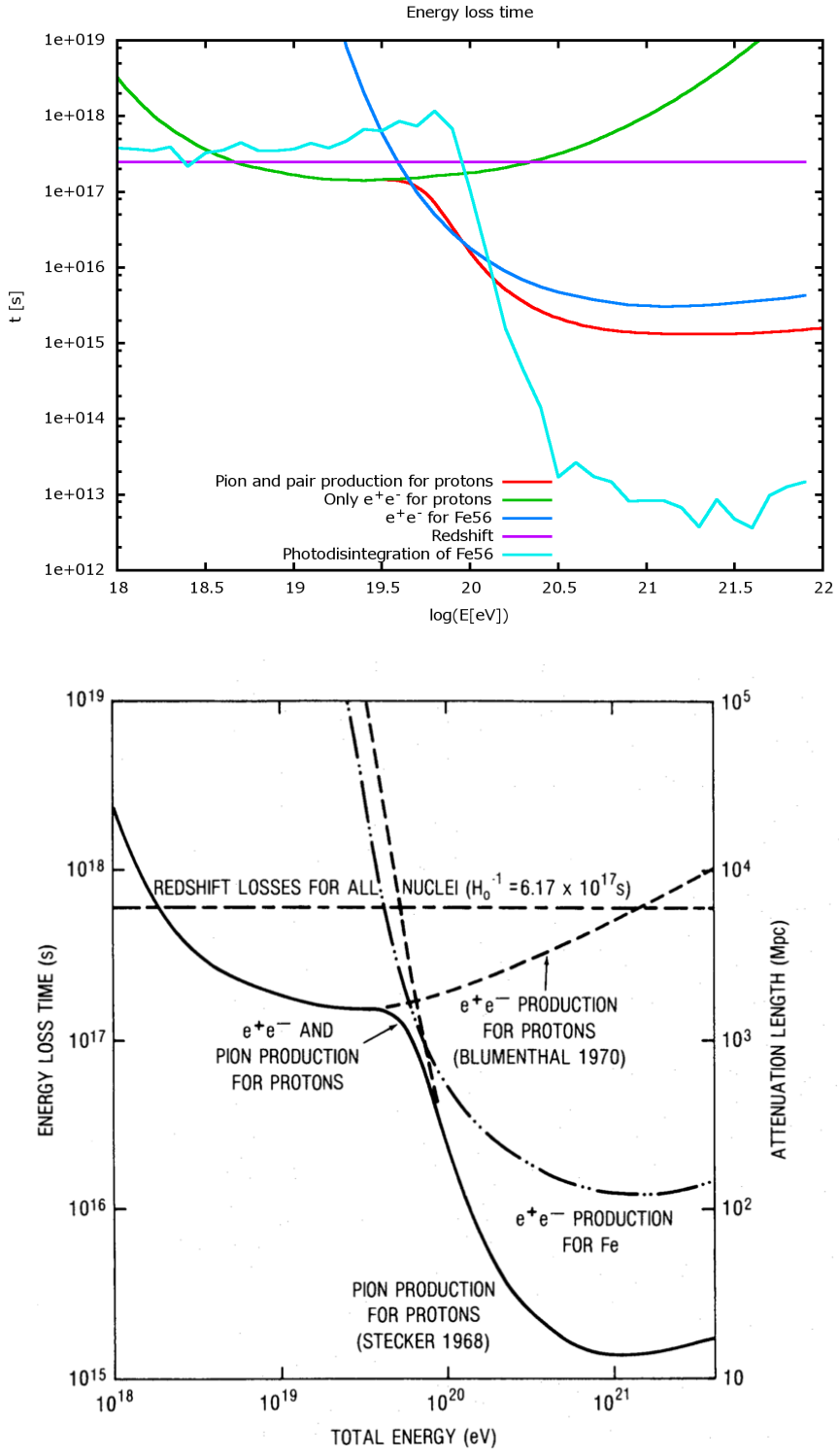

Fig. 4.1: Energy losses from the simulation, compared to the results of Puget *et.al.* [20].

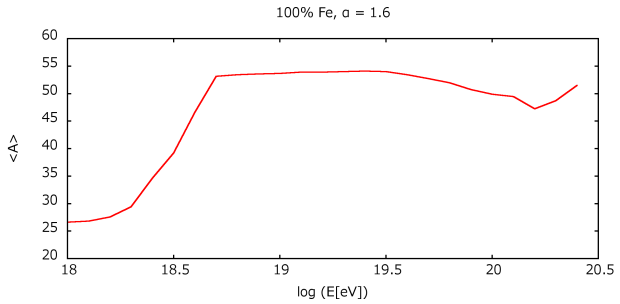

Fig. 4.2: The average atomic weight of the terrestrial composition which started as all iron when injected.

process, which is shown in Fig. 3.1. As expected, the energy loss time remains high, and close to constant, while the mean free path also is long and almost constant at lower energies, and the slope steepens sharply at the same energy in both plots.

Another test of the implementation of photodisintegration is the chemical composition on Earth at different energies. If the injected particles are all iron, we expect that $\langle A \rangle$ should begin to drop when the mean free path as shown in Fig. 3.1 does. At $E \sim E_{\max}$ however, $\langle A \rangle$ could be expected to rise again. Since each final state particle has a lower energy than the initial particle, the only particles left at the very highest energies are those which did not disintegrate more than a few times.

Similarly, since the lighter particles receive a smaller fraction of the initial particle's energy, $\langle A \rangle$ is expected to be lower at the lowest energies, even though the probability of disintegration is small. A proton of $E = 10^{18.0}\,\text{eV}$ corresponds to one ejected in the disintegration of ^{56}Fe of $E = 10^{19.8}\,\text{eV}$, which is approximately the energy at which photodisintegration becomes significant for iron. The result is that photodisintegration will create a large number of lower energy protons, causing the low $\langle A \rangle$ seen at low energies in Fig. 4.2.

4.2 General trends in results

The data sets used as the observational data on Earth in this project is the 2008 results from the Pierre Auger Observatory for $\frac{dN}{dE}$ [26], and the 2010 results for $\langle X_{\max} \rangle$ and $RMS(X_{\max})$ [27].

The energy spectrum of the PAO data is well fitted by $\frac{dN}{dE} \propto E^{-\alpha}$ with $\alpha = 3.0$, as is seen in Fig. 4.3. However, since energy losses increase with

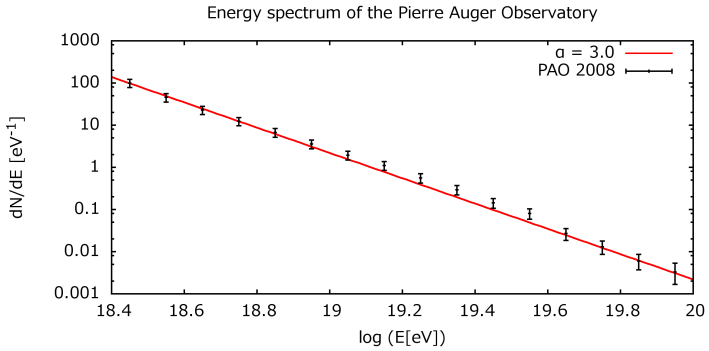

Fig. 4.3: The energy spectrum from the Pierre Auger Observatory.

energy, which will steepen the spectrum before the particles reach Earth, the injected spectrum can have a lower value of α.

When it comes to the EAS, the resulting $\langle X_{\max} \rangle$ and $RMS(X_{\max})$ values from a chemical composition *on the Earth* of only protons and only iron is shown in Fig. 4.4, along with the PAO data. As described in Section 2.5, lighter particles will penetrate further into the atmosphere and have a greater variability in where the maximum is reached, leading to higher values of both $\langle X_{\max} \rangle$ and $RMS(X_{\max})$.

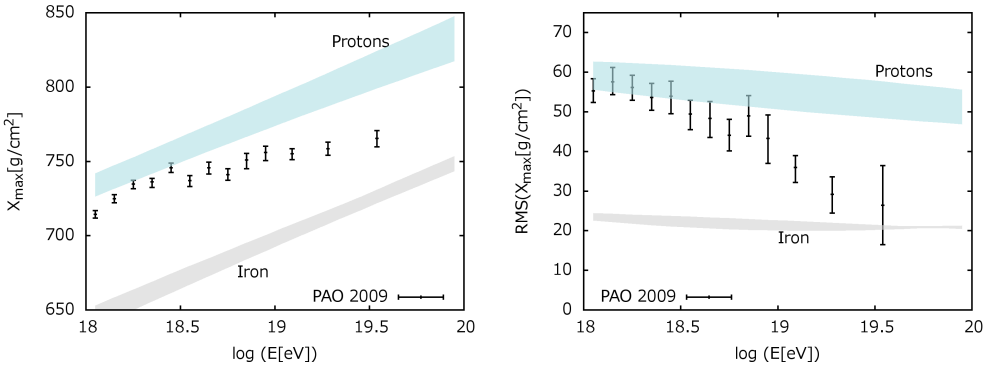

Fig. 4.4: $\langle X_{\max} \rangle$ and $RMS(X_{\max})$ from PAO along with terrestrial compositions of all proton and all iron

The PAO data is close to that of a proton-induced shower up until $E \sim 10^{18.5}$ eV. It differs somewhat from the proton shower between $10^{18.5}$ and 10^{19} eV, and even more after 10^{19} eV. This gives an indication that the chemical composition on Earth consists of lighter nuclei at lower energies

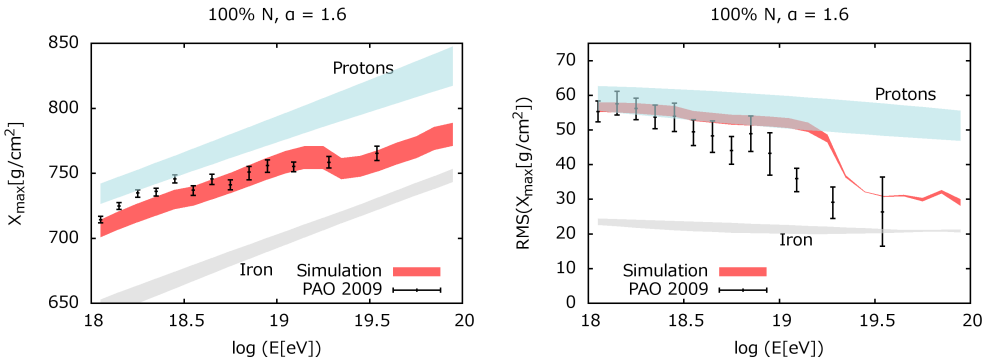

Fig. 4.5: $\langle X_{\max} \rangle$ and $RMS(X_{\max})$ for initial composition 100% nitrogen.

than at higher energies. This is consistent with the results for $\langle A \rangle$ shown in Fig. 4.2. $\langle A \rangle$ only begins to drop again after $E = 10^{20}$ eV, which is outside the range of the PAO data, which only contains one single event above this energy.

As discussed in the previous section, an initial composition made up of only one element will by the time the particles arrive at Earth consist of lighter nuclei at lower energies, and heavier at high energies, except the very highest. Where the change from light to heavier nuclei happens depends on the weight of the initial element. The energy at which this changes happens will here be referred to as the turning point of the composition.

When an iron nucleus of $E = E_{\max}$ disintegrates, an ejected proton will have $E_{\mathrm{p}} = E_{\max}/56$, while a nitrogen nucleus of the same energy will give $E_{\mathrm{p}} = E_{\max}/15$. Therefore, an initial composition of lighter nuclei will create an observed composition which remains light at higher energies than heavier nuclei, with the turning point at an higher energy. Naturally, an initial composition of iron will also lead to a higher maximum value of $\langle A \rangle$ on Earth than one of nitrogen, since the composition on Earth cannot contain *heavier* nuclei than the starting composition. In Fig. 4.5, $\langle X_{\max} \rangle$ and $RMS(X_{\max})$ for an initial chemical composition of only nitrogen is shown, while Fig. 4.8 shows the same for iron.

As can be clearly seen, the turning point is at a lower energy for iron, at $E \sim 10^{18.7}$ eV, than for nitrogen at $E \sim 10^{19.3}$ eV. These plots are both based on an initial energy spectrum of $\alpha = 1.6$. In Fig. 4.6, $\alpha = 2.0$, and in Fig. 4.7 $\alpha = 2.4$. Note that for lower α, the low energy end of the spectrum is closer to a pure proton shower, than for higher values of α, i.e. the composition is lighter. This is due to the fact that the energy spectrum (Eq. (2.9)) for a

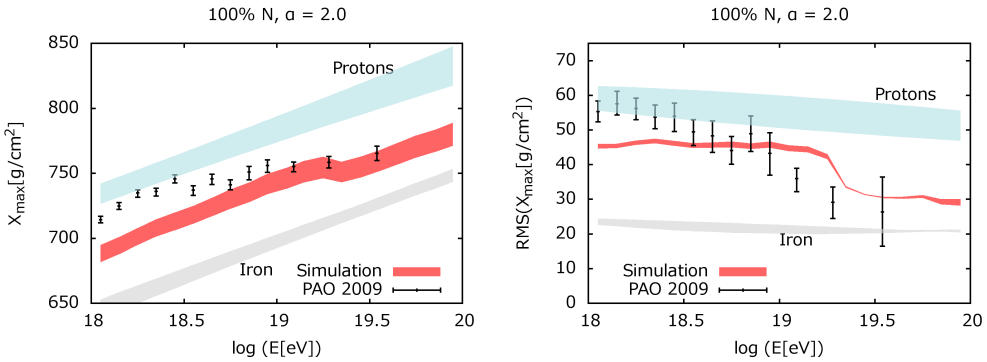

Fig. 4.6: $\langle X_{\max} \rangle$ and $RMS(X_{\max})$ for initial composition 100% nitrogen.

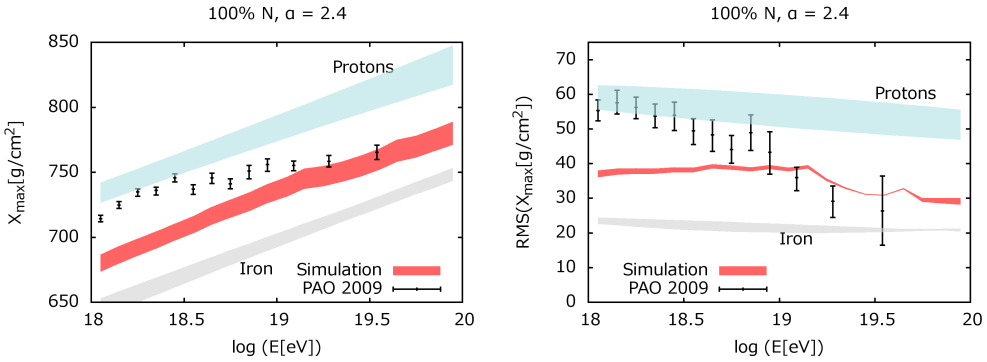

Fig. 4.7: $\langle X_{\max} \rangle$ and $RMS(X_{\max})$ for initial composition 100% nitrogen.

high value of α will be steeper, and with the same $E_{\max}$, a spectrum with a lower value of α will contain more particles in the high end of the energy range, and it is only for particles of high energy that the disintegration, which creates the light composition at lower energies, is likely.

So far, the starting compositions discussed have been made up of only one element. When an admixture of protons is added to a pure injection composition, the characteristics of the shower shift closer to that of a purely proton-induced one, but it does not change the turning point of the composition, as protons are unaffected by photodisintegration. The high energy end of the composition becomes lighter, as without injected protons, there are no protons of high energy.

When an admixture of lighter nuclei are added to for example an all-iron composition, this does alter the turning point. Since all types of nuclei have

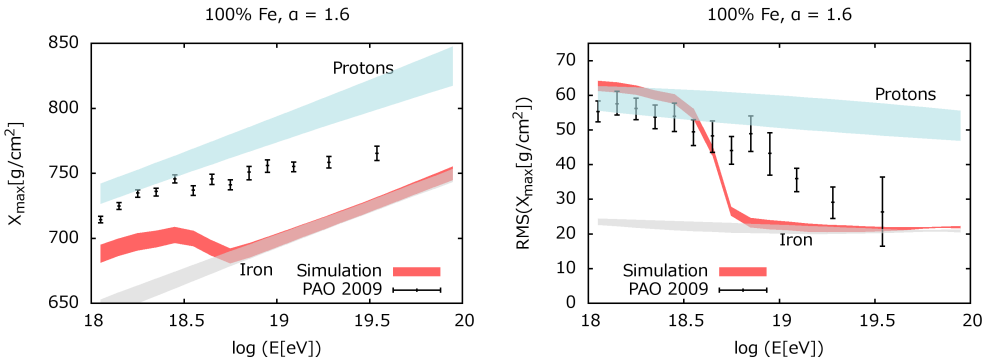

Fig. 4.8: $\langle X_{\max} \rangle$ and $RMS(X_{\max})$ for initial composition 100% iron.

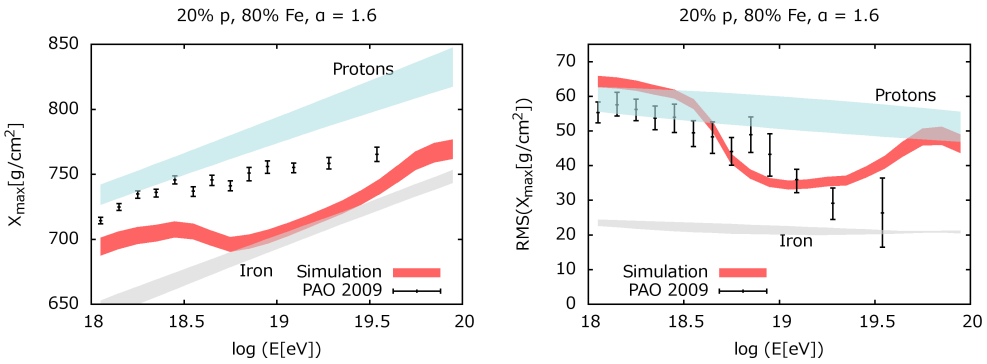

Fig. 4.9: $\langle X_{\max} \rangle$ and $RMS(X_{\max})$ for initial composition 20% p and 80% Fe.

a different energy-dependence of the composition, the change from light to heavy composition will be less abrupt, and happen gradually over a larger energy range when nuclei with different turning points are mixed together. This can be seen when comparing Fig. 4.9, which shows the EAS results for an initial composition of 80% iron and 20% protons, and Fig. 4.10, 50% iron and 50% nitrogen to an initial composition of only iron in Fig. 4.8.

The final variable in this simulation is the maximum energy of the injected particles, $E_{\max}$. This project has mainly focused on the lower $E_{\max} = 10^{20.5}\,\text{eV}$, as this can be considered a more realistic maximum energy, see Section 2.2. However, in case there are sources capable of accelerating particles to even higher energies, some simulations have also been run with $E_{\max} = 10^{22}\,\text{eV}$. An increased value of $E_{\max}$ gives a flattening of the energy spectrum, which means that a higher value of α is needed in order to

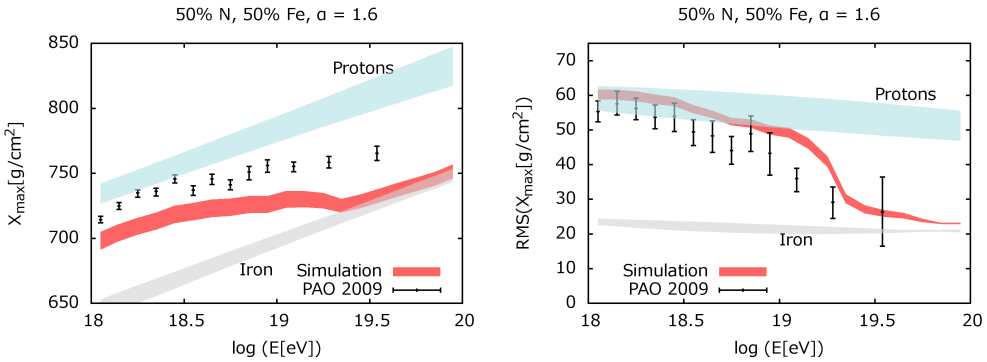

Fig. 4.10: $\langle X_{\max} \rangle$ and $RMS(X_{\max})$ for initial composition 50% N and 50% Fe.

get a good fit to the energy spectrum. In Fig. 4.11 the energy spectrum of a pure nitrogen composition with $\alpha = 1.8$ is shown for both values of $E_{\max}$, to illustrate this difference.

An increased maximum energy also affects the chemical composition observed on Earth drastically. As has already been discussed, the terrestrial composition will become heavier at energies above $E \sim 10^{19}$eV when $E_{\max} = 10^{20.5}$eV, because photodisintegration cannot create protons above $E_{\mathrm{p}} = E_{\max}/A$. When $E_{\max} = 10^{22}$, even disintegration of heavy nuclei can create protons of energies up to 10^{20}eV. This lightens the terrestrial chemical composition throughout the energy range of the PAO data, and as can be seen in Fig. 4.12, the composition becomes too light, even for an initial composition of iron.

4.3 Best results

The goodness of fit test described in Section 2.6 gives an indication of how well the simulated data fit to the PAO data. However, in the case of $\langle X_{\max} \rangle$ and $RMS(X_{\max})$ the expected value, i.e. the simulated one, is a range, not one single value. The observed values from the PAO have, in all three cases, quite large uncertainties, especially at the highest energies. Even a result which yields a high value of χ^2 can be close to, or even within, the error bars. As such, the χ^2-test should not be taken as a definite way of rejecting a hypothesis in this case, but as an indication of which hypothesis looks more promising.

When it comes to the EAS, we expect from the discussion in the previous section that the best terrestrial composition is one which is light at the lower

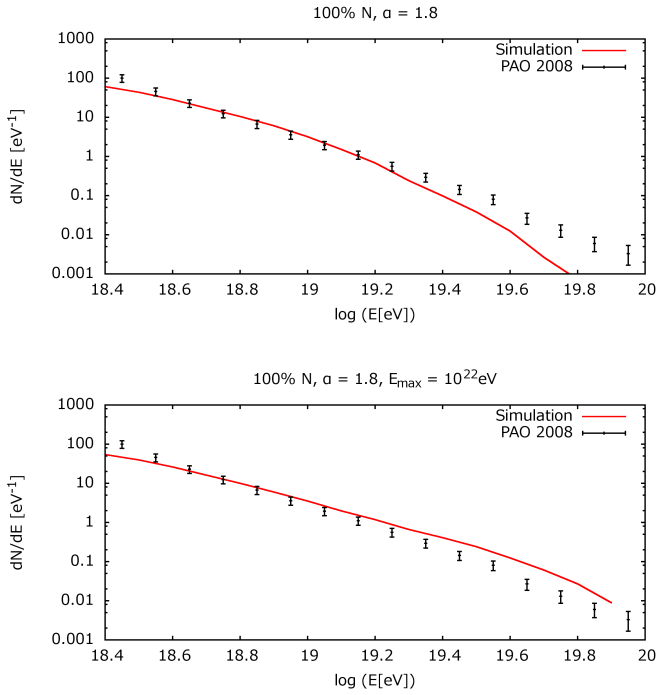

Fig. 4.11: Energy spectrum for different $E_{\max}$.

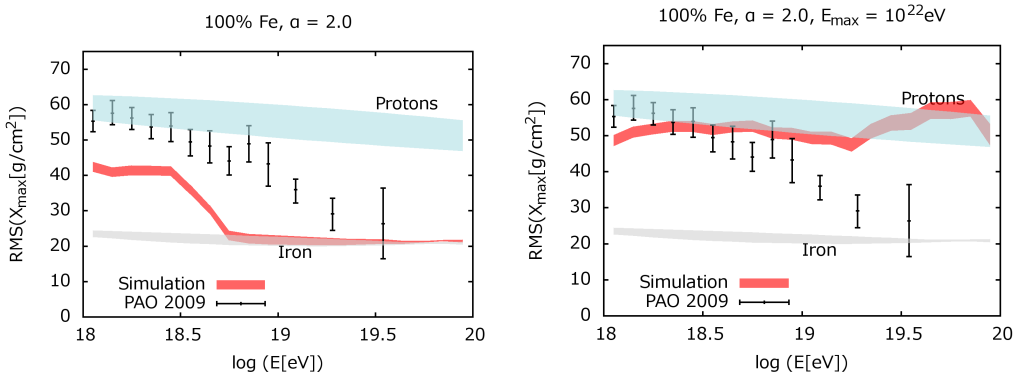

Fig. 4.12: $RMS(X_{\max})$ for different $E_{\max}$

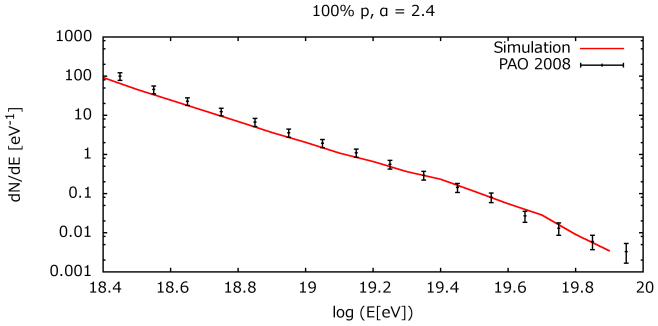

Fig. 4.13: Energy spectrum for a pure proton composition

end of the energy range, medium-weight at the higher end, and without a sharp change in weight. This indicates an initial composition made of up several types of nuclei, to achieve the slower change of weight, but no protons, to ensure that the terrestrial composition does not become too light at high energies, as seen in Fig. 4.9.

As mentioned above, the χ^2 test is not used in exactly the way described in Section 2.6 in this simulation. Because of the range of values of $\langle X_{\max} \rangle$ and $RMS(X_{\max})$, even a data set with a quite poor fit can yield a χ^2-value below the critical, and for $\frac{dN}{dE}$, a data set which is close to being within the error bars of the PAO data can still have a very high value of χ^2. In this section χ^2_E,χ^2_X and χ^2_R refer to the χ^2-values for the energy spectrum, $\langle X_{\max} \rangle$ and $RMS(X_{\max})$ respectively.

For the energy spectrum, none of the various combinations of α and chemical composition gave a fit below the critical value of χ^2. In general, all χ^2-values for the energy spectrum are very high in this project. Good examples are shown in Fig. 4.13, which shows the energy spectrum for a pure proton composition with $\alpha = 2.4$, and Fig. 4.14 which shows the EAS data for 20% protons and 80% silicon at $\alpha = 1.8$. Pure protons with $\alpha = 2.4$ was the best fit achieved to the energy spectrum, and is a quite reasonable fit, but still with $\chi^2_E = 151.7$. The proton and silicon combination however, clearly shows that while it stays close to observed data in the lower part of the energy range, at least for $RMS(X_{\max})$, it develops in a drastically different way than the PAO data set does, but still its $\chi^2_X = 5.621$ and $\chi^2_R = 11.013100$.

The starting conditions which give the best fits to the energy spectrum, $\langle X_{\max} \rangle$ and $RMS(X_{\max})$ are all different, and it is not possible to find one starting condition which provides an satisfactory fit to all three observables on the Earth. However, there are several possibilities which come close, and all provide similarly good fits. In Table 4.1 the χ^2-values of several of the best fits

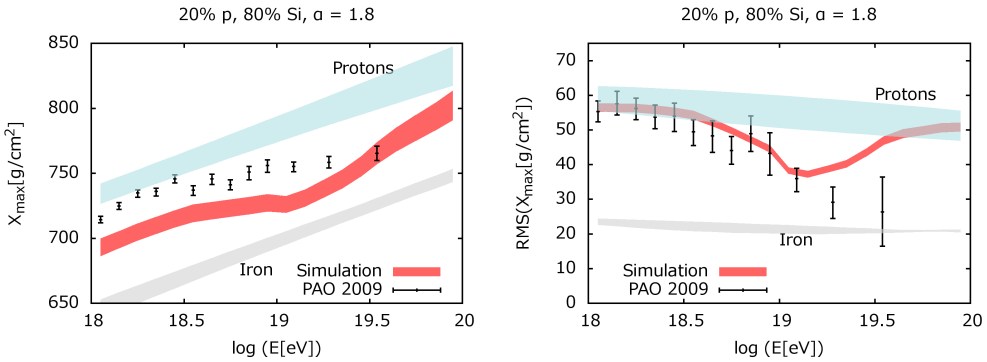

Fig. 4.14: $\langle X_{\max} \rangle$ and $RMS(X_{\max})$ for initial composition 20% p and 80% Si.

are listed. The critical value of χ^2 for the energy spectrum is $\chi^2_{cr} = 23.6848$ (14 degrees of freedom), and for both $\langle X_{\max} \rangle$ and $RMS(X_{\max})$, $\chi^2_{cr} = 21.0261$ (12 degrees of freedom).

As can clearly be seen from the tabulated χ^2-values, injecting only protons, with a high value of $\alpha = 2.4$ gives by far the best fit for the energy spectrum. In general, a lighter chemical composition, preferably with a high proton content, and a higher value of α gives better fits to the energy spectrum. However, it is clear from the previous discussions that the EAS data will much better fitted by a medium-weight chemical composition, ideally without any proton content at all. It is the EAS data which is actually observed on Earth, and the energy spectrum calculated from that data. As discussed in Section 2.5, there are several models, and therefore several possible ways of doing this. It has been suggested that the energy measured by the PAO should be increased by approximately 30% [7]. For this reason, the conclusions of this study are based more on the EAS data than the energy spectrum.

The best fits to the EAS data are combinations of nitrogen and silicon, and to a certain extent, a pure silicon or nitrogen composition. The combinations tested were 25% N + 75% Si and 50% N + 50% Si. It can be seen both from the plots and the χ^2-values that these are not very good fits to the energy spectrum however. A lower value of α gives a better fit to the EAS data, but at the same time gives an even poorer fit to the energy spectrum.

The results from an injection spectrum of only silicon is shown in Fig. 4.15. The shape of EAS data graphs is very close to that of the observed data from PAO. However, the composition is too heavy throughout the energy range. As was discussed in Section 4.2, a lower α-value would shift the composition to a lighter one, but at the same time, worsening the fit to the energy spectrum,

Tab. 4.1: χ^2-values for selected starting conditions, all with $E_{\max} = 10^{20.5}$ eV

α	% p	% N	% Si	% Fe	χ^2_E	χ^2_X	χ^2_R
1.6	20	10	10	60	4855.47	11.55	2.89
1.6	0	100	0	0	4033.79	0.24	13.55
1.6	0	0	100	0	4046.82	3.82	4.51
1.6	0	50	50	0	3958.91	0.83	7.80
1.6	0	25	75	0	3948.54	1.94	3.96
1.6	0	20	20	60	4855.47	11.55	2.89
1.8	20	0	80	0	3644.78	5.62	11.01
1.8	20	10	10	60	4142.37	20.71	0.67
1.8	0	100	0	0	3198.29	1.83	10.16
1.8	0	0	100	0	3780.89	9.66	2.70
1.8	0	50	50	0	3367.51	4.22	3.95
1.8	0	50	0	50	3649.81	12.76	2.91
1.8	0	25	75	0	3478.42	6.54	1.23
1.8	0	20	20	60	4142.37	20.71	0.67
2.0	0	50	50	0	2463.29	9.37	9.96
2.0	0	25	75	0	2694.13	12.87	9.51
2.2	20	20	40	20	1429.94	15.62	14.65
2.4	100	0	0	0	151.70	5.18	25.13

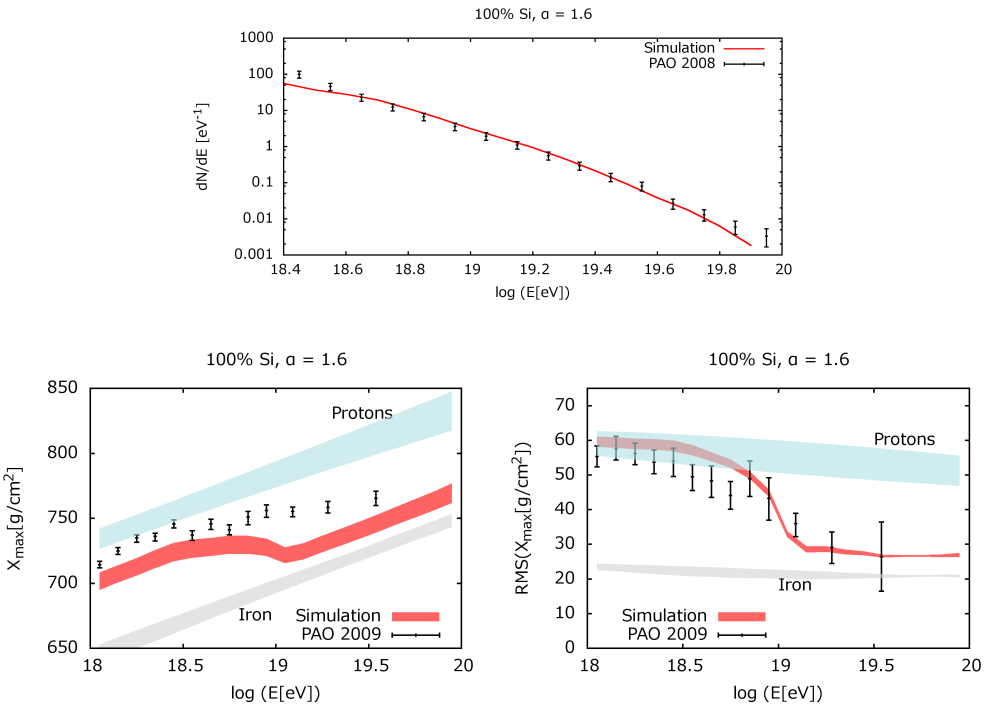

Fig. 4.15: The results of injecting only silicon, $\alpha = 1.6$.

causing it to drop off too quickly at the high energy end of the range.

The results from pure nitrogen was shown in the previous section, in Fig. 4.5. It is a very good fit to $\langle X_{\max} \rangle$, but a poorer fit to $RMS(X_{\max})$, and a poorer fit overall than the heavier compositions which also contain silicon.

Results for the combinations of nitrogen and silicon are shown on the next pages. A larger fraction of silicon gives a better result for $RMS(X_{\max})$, while a larger fraction of nitrogen gives better results for the energy spectrum and $\langle X_{\max} \rangle$. The lowest sum of $\chi^2_X + \chi^2_R$ is that of the 25% N + 75% Si starting composition at $\alpha = 1.6$. Since both 100% Si and 50% N + 50% Si give promising results, it is perhaps not unexpected that the combination 25% N + 75% Si yields the best results.

The fit for $RMS(X_{\max})$ for 25% N + 75% Si is better for $\alpha = 1.8$ than $\alpha = 1.6$. However, the fit to $\langle X_{\max} \rangle$ favours the lower value, and since the uncertainties in the measurements are relatively larger for $RMS(X_{\max})$ a larger value of χ^2 is more acceptable here than for $\langle X_{\max} \rangle$. In addition the overall error is smaller for the lower α.

There is one combination with iron which also gives a somewhat promising result; 20% N, 20% Si and 60% Fe. However this is a good fit to $RMS(X_{\max})$,

but a poor fit to $\langle X_{\mathrm{max}} \rangle$, as can be seen in Table 4.1. It is still an interesting result, because it is unrealistic that an environment which contains a large amount of silicon contains no iron at all, as they are created in the second to last and last possible stage of stellar fusion, respectively. If, for example, the source of cosmic ray particles is a supernova explosion, it will contain iron as well as silicon.

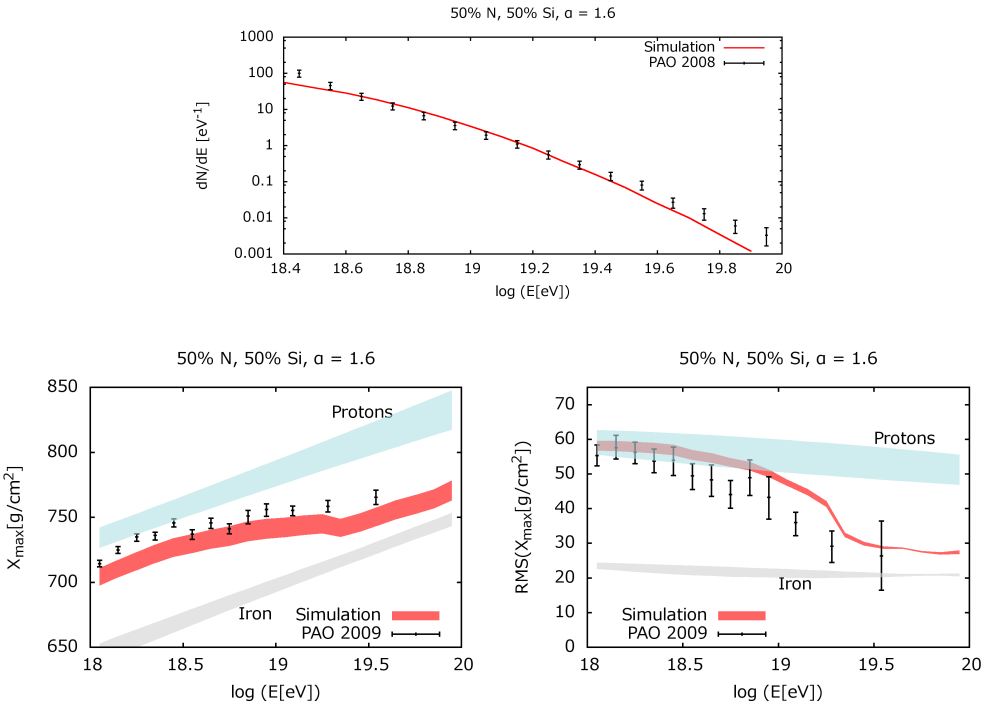

Fig. 4.16: Silicon and nitrogen mix, $\alpha = 1.6$

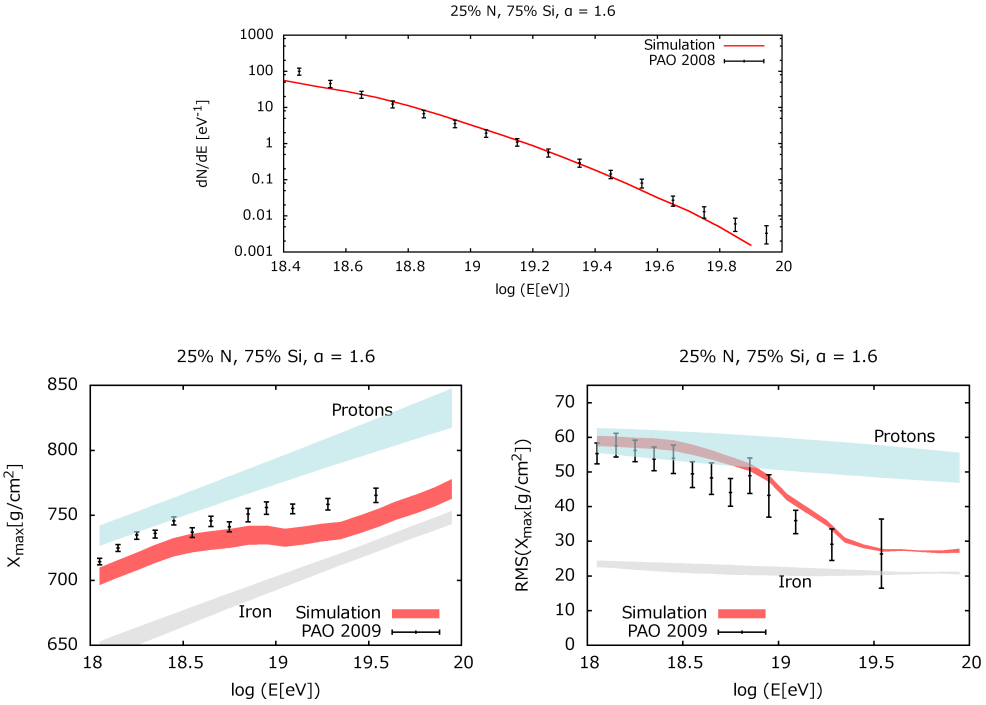

Fig. 4.17: Silicon and nitrogen mix, $\alpha = 1.6$

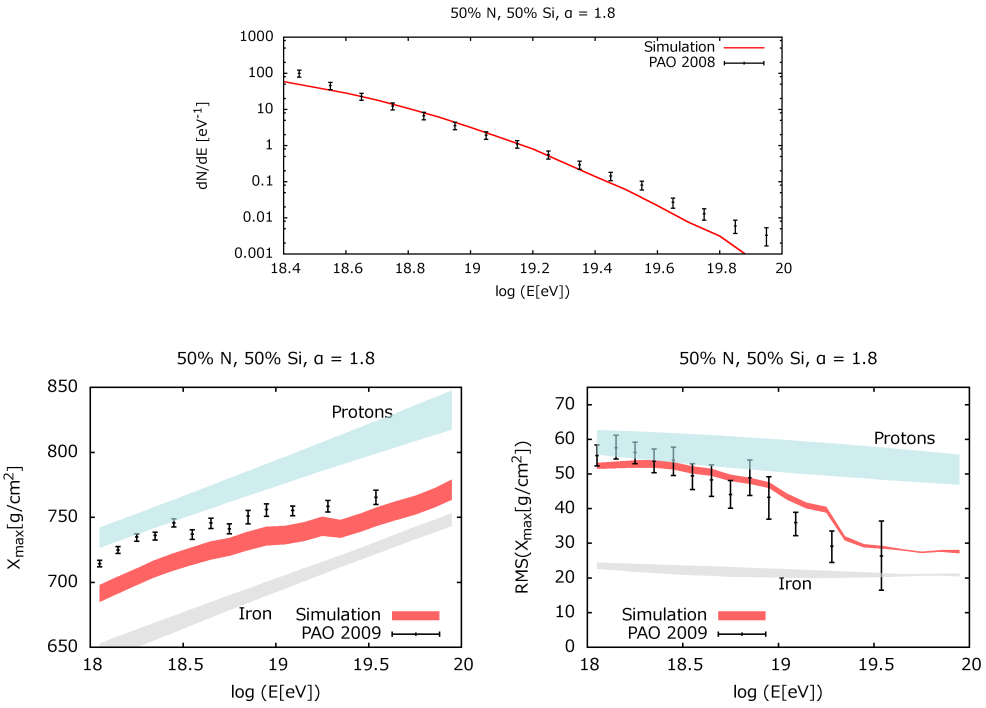

Fig. 4.18: Silicon and nitrogen mix, $\alpha = 1.8$

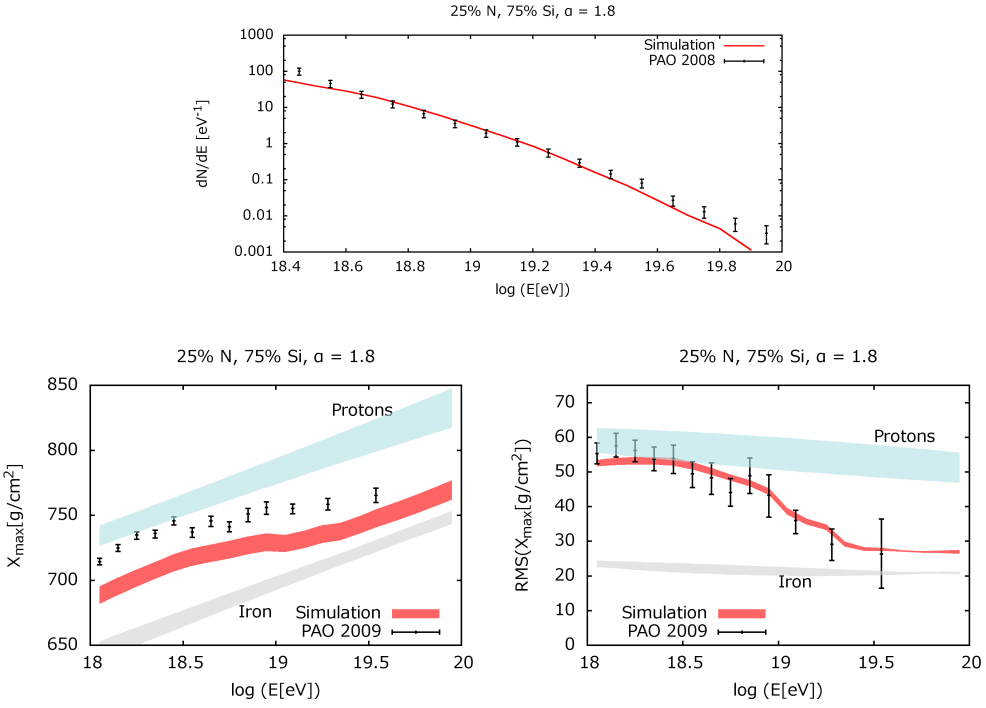

Fig. 4.19: Silicon and nitrogen mix, $\alpha = 1.8$

5. CONCLUSION

In this project a Monte Carlo simulation of the propagation of UHECRs have been used to investigate which initial conditions provide the best results for the data observed on Earth by the Pierre Auger Observatory. For sources distributed uniformly in comoving distance from the Earth, injecting particles of an energy spectrum $\frac{dN}{dE} \propto E^{-\alpha}$ a mixed initial chemical composition consisting of medium-weight nuclei and $\alpha = 1.6 - 1.8$ gives the best results.

It has not been possible to find one starting condition which gives good results for both $\frac{dN}{dE}$, $\langle X_{\max} \rangle$ and $RMS(X_{\max})$. Taylor and Hooper's results [12] suggest that by considering the extra-galactic magnetic field, which was beyond the scope of this project. The results of this project are in general agreement with Taylor and Hooper's, both results support an initial composition of medium-weight nuclei and a quite low $\alpha = 1.6 - 1.8$.

This could resolve the apparent contradiction that the fit to $\frac{dN}{dE}$ worsens as the fit to $\langle X_{\max} \rangle$ and $RMS(X_{\max})$ improves and vice versa. But the difficulty of finding starting conditions which yield results which fit all the observed data could also be an indication that the error margins in the observed data are underestimated, or even that there are problems with the models used to calculate $\frac{dN}{dE}$, $\langle X_{\max} \rangle$ and $RMS(X_{\max})$ from the raw observational data.

One problem with this result is that it is implausible to have an initial chemical composition consisting only of medium-weight nuclei without any iron at all. However, compositions which contained iron were among the second-best, but they only provided a good fit to one data set, $RMS(X_{\max})$.

The lower $E_{\max} = 10^{20.5}\,\text{eV}$ gave better results than $E_{\max} = 10^{22}\,\text{eV}$, strengthening the claim made in Section. 2.2 that $10^{20.5}\,\text{eV}$ is the more realistic maximum energy to which the sources can accelerate UHECRs. The results also show that the initial chemical composition should not contain any significant amount of protons. This could be an indication that the electromagnetic fields of the sources are of sufficient strength to accelerate nuclei of $Z \sim 10$ to $E_{\max}$, but not protons.

Acknowlegdements I would like to thank Michael Kachelrieß, my thesis advisor, for his help, and Sergey Ostapchenko and Askhat Gazizov for providing code for calculations of EAS and photodisintegration.

BIBLIOGRAPHY

[1] E.J. Ahn, R. Engel, T. Gaisser, P. Lipari, and T. Stanev. Cosmic ray interaction event generator SIBYLL 2.1. *Physical Review D*, 80(9):1–17, 2009.

[2] D. Allard, A.V. Olinto, and E. Parizot. Signatures of the extragalactic cosmic-ray source composition from spectrum and shower depth measurements. *Astronomy & Astrophysics*, 473(1), 2007. arXiv:0703633v2 [astro-ph].

[3] P. Auger, P. Ehrenfest, R. Maze, J. Daudin, and R.A. Fréon. Extensive cosmic-ray showers. *Reviews of Modern Physics*, 11(3-4):288–291, 1939.

[4] G.R. Blumenthal. Energy loss of high-energy cosmic rays in pair-producing collisions with ambient photons. *Physical Review D*, 1(6):1596–1602, 1970.

[5] T.M. Davis and C.H. Lineweaver. Expanding Confusion: common misconceptions of cosmological horizons and the superluminal expansion of the Universe. *Publications of the Astronomical Society of Australia*, 21(1):26, 2003.

[6] D. De Marco. On the statistical significance of the GZK feature in the spectrum of ultra-high energy cosmic rays. *Astroparticle Physics*, 20(1):53–65, 2003.

[7] R. Engel and The Pierre Auger Collaboration. Test of hadronic interaction models with data from the Pierre Auger Observatory.
30th International Cosmic Ray Conference, 2007.
arXiv:0706.1921v1 [astro-ph].

[8] C. Amsler et. al. (Particle Data Group). Review of particle physics. *Physics Letters B*, 667, 2008.

[9] K. Greisen. End to the cosmic-ray spectrum? *Physical Review Letters*, 16(17):748–750, 1966.

[10] J.B. Hartle. *Gravity: An Introduction to Einstein's General Relativity.* Addison Wesley, 2003.

[11] D.W. Hogg. Distance measures in cosmology. arXiv:9905116v4 [astro-ph], 2000.

[12] D. Hooper and A.M. Taylor. On the heavy chemical composition of the ultra-high energy cosmic rays. *Astroparticle Physics*, 33(3):151–159, April 2010.

[13] T. et.al. Kalliokoski. Can EMMA solve the puzzle of the knee? *Progress in Particle and Nuclear Physics*, 66(2):468–472, 2011.

[14] N. Kalmykov, S. Ostapchenko, and A. Pavlov. Quark-gluon-string model and EAS simulation problems at ultra-high energies. *Nuclear Physics B - Proceedings Supplements*, 52(3):17–28, 1997.

[15] T.M. Kneiske and H. Dole. A Lower-Limit Flux for the Extragalactic Background Light. *Astronomy & Astrophysics*, 515, 2010.

[16] J. Matthews. A Heitler model of extensive air showers. *Astroparticle Physics*, 22(5-6):387–397, 2005.

[17] S. Ostapchenko. QGSJET-II: towards reliable description of very high energy hadronic interactions. *Nuclear Physics B - Proceedings Supplements*, 151(1):143–146, 2006.

[18] S. Ostapchenko. Status of Air Shower Simulations. 2010. arXiv:1010.0137v2 [astro-ph.HE].

[19] W.H. et al Press. *Numerical Recipes.* Cambridge University Press, 3rd edition, 2007.

[20] J.L. Puget, F.W. Stecker, and J.H. Bredekamp. Photonuclear interactions of ultrahigh energy cosmic rays and their astrophysical consequences. *The Astrophysical Journal*, 205:638–654, 1976.

[21] R. Schlickeiser. *Cosmic Ray Astrophysics.* Springer, 2002.

[22] Y. Sekido and H. Elliot. *Early History of Cosmic Ray Studies: Personal reminiscences with old photographs (Astrophysics and Space Science Library).* Springer, 1985.

[23] T. Stanev. *High Energy Cosmic Rays (Springer Praxis Books / Astronomy and Planetary Sciences).* Springer, 2nd edition, 2010.

[24] F.W. Stecker. Effect of photomeson production by universal radiation field on high-energy cosmic rays. *Physical Review Letters*, 21(14):1016–1018, 1968.

[25] F.W. Stecker. Photodisintegration of Ultrahigh-Energy Cosmic Rays by the Universal Radiation Field. *Physical Review*, 180(5):1264–1266, 1969.

[26] The Pierre Auger Collaboration. Observation of the Suppression of the Flux of Cosmic Rays above 4e19 eV. *Physical Review Letters*, 101(6):7, 2008.

[27] The Pierre Auger Collaboration. Measurement of the Depth of Maximum of Extensive Air Showers above 10^{18} eV. *Physical Review Letters*, 104(9), 2010.

[28] R.E. Walpole, R.H. Myers, S.L. Myers, and K. Ye. *Probability and statistics for scientists and engineers*. Pearson Education, 8th edition, 2007.